Variations in the Three-Dimensional Structure of the Atmospheric Circulation with Different Flavors of El Niño

KEVIN E. TRENBERTH AND LESLEY SMITH

National Center for Atmospheric Research, Boulder, Colorado*

(Manuscript received 23 June 2008, in final form 22 October 2008)

ABSTRACT

Two rather different flavors of El Niño are revealed when the full three-dimensional spatial structure of the temperature field and atmospheric circulation monthly mean anomalies is analyzed using the Japanese Reanalysis (JRA-25) temperatures from 1979 through 2004 for a core region of the tropics from 30°N to 30°S, with results projected globally onto various other fields. The first two empirical orthogonal functions (EOFs) both have primary relationships to El Niño–Southern Oscillation (ENSO) but feature rather different vertical and spatial structures. By construction the two patterns are orthogonal, but their signatures in sea level pressure, precipitation, outgoing longwave radiation (OLR), and tropospheric diabatic heating are quite similar. Moreover, they are significantly related, with EOF-2 leading EOF-1 by about 4–6 months, indicating that they play complementary roles in the evolution of ENSO events, and with each mode playing greater or lesser roles in different events and seasons.

The dominant pattern (EOF-1) in its positive sign features highly coherent zonal mean warming throughout the tropical troposphere from 30°N to 30°S that increases in magnitude with height to 200 hPa, drops to zero about 100 hPa at the tropopause, and has reverse sign to 30 hPa with peak values at 70 hPa. It correlates strongly with global mean surface temperatures. EOF-2 emphasizes off-equatorial centers of action and strong Rossby wave temperature signatures that are coherent throughout the troposphere, with the strongest values in the Pacific that extend into the extratropics and a sign reversal at and above 150 hPa. Near the surface, both patterns feature boomerang-shaped opposite temperatures in the western tropical and subtropical Pacific, with similar sea level pressure patterns, but with EOF-1 more focused in equatorial regions. Both patterns are strongest during the boreal winter half-year when anomalous precipitation in the tropics and associated latent heating drive teleconnections throughout the world. For El Niño in northern winter EOF-1 has more precipitation in the eastern tropical Pacific, while EOF-2 has much drier conditions over northern Australia and the Indian Ocean. In northern summer, the main differences are in the South Pacific and Indian Ocean. Differences in teleconnections suggest great sensitivity to small changes in forcings in association with seasonal variations in the mean state.

1. Introduction

The main source of interannual variability in the climate system is from El Niño–Southern Oscillation (ENSO), which has its core in the air–sea interactions in the tropical Pacific. A key question is whether the differences in character among the different El Niño events matter in terms of their impacts on the atmospheric circulation and teleconnections and especially in terms of impacts on society (Kumar et al. 2006). In other words, do the different ''flavors'' of El Niño matter and how can we best characterize them?

An empirical orthogonal function (EOF; otherwise known as a principal component) analysis of sea surface temperatures (SSTs) brings out the dominant ENSO pattern that is well represented by the Niño-3.4 index as the area-average SST anomalies over 5°N–5°S, 170°–120°W (Trenberth and Stepaniak 2001). However, this does not capture the evolution of the SST fields (Trenberth et al. 2002b), and the second EOF of SSTs has been characterized as the Trans-Niño Index (TNI) (Trenberth and Stepaniak 2001; Kumar et al. 2006) as it depicts

* The National Center for Atmospheric Research is sponsored by the National Science Foundation.

Corresponding author address: Kevin E. Trenberth, National Center for Atmospheric Research, P.O. Box 3000, Boulder, CO 80307-3000.
E-mail: trenbert@ucar.edu

DOI: 10.1175/2008JCLI2691.1

normalized SST differences between the date line (Niño-4 region) and South American coast (Niño 1 + 2 region). This second pattern has also been referred to as the ''El Niño Modoki'' by Ashok et al. (2007) and as the ''central Pacific ENSO'' by Kao and Yu (2009). These two indexes have changes in precipitation and outgoing longwave radiation (OLR) associated with ENSO identified with them (Trenberth et al. 2002a).

Another view emerges as the full three-dimensional structure of ENSO is taken into account. By analyzing the full three-dimensional temperature structure of the atmosphere, Trenberth and Smith (2006) found two distinctly different flavors of El Niño whose surface signatures were more similar than different in terms of temperatures and sea level pressures. They performed an analysis of the full three-dimensional spatial structure of the temperature field monthly mean anomalies from the 40-yr European Centre for Medium-Range Weather Forecasts (ECMWF) Re-Analysis (ERA-40) for a core region of the tropics from 30°N to 30°S, with results projected globally. However, as they also identified some substantial inhomogeneities in the ERA-40 reanalysis that affected the results, it is important to replicate the results using the recent independent Japanese reanalysis (JRA-25; Onogi et al. 2007). The purpose of this paper is to do this and extend the analysis to examine seasonal variations.

In Trenberth and Smith (2006) the dominant pattern (EOF-1), in its positive sign, featured highly coherent zonal mean warming throughout the tropical troposphere from 30°N to 30°S that increases in magnitude with height to 300 hPa and reverses sign above about 100 hPa at the tropopause to 30 hPa. Spatially at low levels it showed warmth throughout most of the tropics although with weak or slightly opposite sign in the western tropical Pacific and a strong reversed sign in the Pacific subtropics. The coherent structure features waves below 700 hPa at higher latitudes but is more zonal above there with off-equatorial maxima straddling the equator in the eastern Pacific in the upper troposphere and opposite sign at 100 hPa. The corresponding sea level pressure pattern is similar to but more focused in equatorial regions than the Southern Oscillation pattern. The time series highlights the 1997/98 El Niño, along with those in 1982/83 and 1986/87 and the 1988/89 La Niña, and correlates strongly with global mean surface temperatures. All of these aspects are reproduced in the current study.

Missing, however, in the Trenberth and Smith (2006) EOF-1 result were the prolonged sequence of 3 successive El Niño events in the early 1990s, which were instead highlighted in EOF-3 as part of a mainly lower-frequency decadal variation that features modest zonal mean features owing to cancellation around latitude circles. This mode also shows up in our current analysis but in somewhat modified form. Spatially at the surface this pattern is dominated by Southern Oscillation wave 1 structures throughout the tropics and especially the subtropics. The regional temperature structures are coherent throughout the troposphere, with the strongest values in the Pacific extending well into the extratropics, and with a sign reversal above 100 hPa. Strong Rossby wave signatures are featured in the troposphere with a distinctive quadrupole pattern that reverses at 100 hPa. The quite different three-dimensional structure of these patterns highlights the need to consider the full structure outside of the Pacific and at all vertical levels in accounting for impacts of ENSO and how they relate to the global mean.

In the ERA-40 temperature analysis, EOF-2 had a complex vertical structure and was thought to be largely spurious and associated with problems in assimilating satellite data. The inhomogeneities in the ERA-40 data left questions open about how much contamination of the results had occurred especially from the problems of assimilating radiances in the presence of the aerosol from the Mount Pinatubo volcanic eruption in 1991 (Uppala et al. 2005). Accordingly, it is of interest to reexamine these results using JRA-25, which starts in 1979 and runs through 2004. Results presented below show that the two ENSO-related patterns now emerge as the first two patterns, which confirms that the previous EOF-2 was indeed spurious. However, the new results appear to be improved in other respects, and there are also some interesting differences in the second pattern.

Accordingly, we have used the new time series to document other ancillary correlated fields of precipitation and OLR associated with the two flavors of El Niño. This paper also breaks the patterns down by season, although it is found that this can be done reasonably well with just two extended seasons corresponding to the northern winter from November to March (NDJFM) and summer from May to September (MJJAS), leaving April and October as transition months.

Section 2 briefly describes the main analysis, and section 3 presents the results. Section 4 discusses these in the context of previous studies and presents the conclusions.

2. Methods and data

An evaluation of the JRA-25 analyses (Onogi et al. 2007; Trenberth and Smith 2008) shows that, while they do not suffer from the problem with contamination of radiances from aerosol from the Mount Pinatubo eruption in 1991 in ERA-40, they nonetheless contain

some discontinuities associated with changes in the observing system. The effects are relatively small compared with the main signals sought here, but they may nevertheless quantitatively affect the time series.

Monthly mean temperature anomalies were computed relative to a climatology for 1979 to 2004 at each of the pressure levels in the JRA-25 archive. These include 11 levels from 1000 to 200 hPa as well as the 150-, 100-, 70-, 50-, 30-, and 10-hPa levels. We use the data at T63 resolution on a Gaussian grid, which corresponds to a grid of approximately 1.875°. We use EOF analysis of all monthly anomalies combined but focus on a core region of the tropics and subtropics (30°N–30°S).

To perform the EOF analysis, as in Trenberth and Smith (2006), nine levels are selected (1000, 850, 700, 600, 500, 400, 300, 200, and 100 hPa) as primary levels for the analysis, and we use every second grid point in longitude, for a total of 27 648 grid points. Values are weighted by the square root of the cosine of latitude to account for convergence of meridians. Then, results are projected onto all levels and the global domain using regression. The vertical resolution is therefore about 100 hPa; below 700 hPa we might have used 800- and 900-hPa levels but, as these are not available, we use the 850- and 1000-hPa levels (which still allows 3 levels for a 300-hPa layer). This also has the advantage of essentially depicting the SST patterns in temperature anomalies at 1000 hPa. We also performed analyses with other mixes of levels and results do not change much.

The EOF analysis was performed with the correlation matrix, which effectively normalizes each grid point by its standard deviation, to emphasize covariability.

Trenberth and Smith (2006) presented the zonal mean of the standard deviations of monthly anomalies as a cross section and standard deviations at 850, 500, and 200 hPa. Variability is least in the tropics and patterns are predominantly zonally symmetric. Largest values occur over extratropical continents at low levels and generally increase with height to become a maximum at 10 hPa in the extratropical stratosphere of both hemispheres. For 1979–2004 there are 26 yr of monthly anomalies, 312 values, for which the correlation would need to exceed 0.11 to be significant at the 5% level if all values were independent. If only every third value is independent this increases to 0.20, and we regard this as a reasonable threshold for values worthy of further consideration.

Although the analysis is of the continuous monthly time series, there is clearly a strong seasonality to the results and accordingly, and we extract the monthly time series and reconstruct the associated temperature and circulation patterns for each month. Rather than show 12 of everything, these are further condensed into two main seasons (NDJFM, MJJAS), as is justified further below.

3. Results

a. Time series

The EOF analysis results for the first EOF, with 25.1% of the normalized temperature variance from 30°N to 30°S, is very similar to that in the Trenberth and Smith (2006) analysis with the ERA-40 data. The second EOF accounts for 9.4% of the variance, and the third EOF accounts for only 4.8% of the variance, so the first two EOFs are distinct and well separated, and the third and higher EOFs are less coherent in structure and spatial time scale. For comparison, the ERA-40 results had the first 3 EOFs with 22.2%, 9.4%, and 8.4% of the variance. Hence the second EOF, which depicted spurious variability, has now disappeared so that the total variance is reduced and the fraction of the variance accounted for by the remaining two EOFs is now increased slightly. This provides further justification for focusing on them.

Figure 1 presents the time series of these two EOFs along with that of the normalized Niño-3.4 SST index, where the latter has a 5-month running mean applied to anomalies of SSTs. EOF-1 features the 1997/98 El Niño event most prominently, but also includes the 1982/83 and 1986/87 events along with the 1984/86, 1988/89, and 1999/2000 La Niña cold events. EOF-2 also features the 1982/83 El Niño event along with the 1992–95 prolonged event (or series of events; Trenberth and Hoar 1996, 1997). It has some component of the 1997/98 event and prominently features the 1988/89 and 1999 cold events. Accordingly, it is the 1992–95 warm event and the 1999–2002 cool conditions that strongly discriminate between the two time series, whereas both EOFs contribute to the 1982/83, 1986/87, and 1997/98 events. The weak events in 2002 and 2003 are mainly in evidence in EOF-1. However, although the two EOFs often both contribute to ENSO events, there is a strong tendency for EOF-2 to lead EOF-1, so that for the full 1979 to 2004 period the highest statistically significant cross correlation of $r = 0.41$ is with EOF-2 leading by 4 months. Nevertheless, the overall best relationship is with EOF-2 leading by about 6 months when all lead–lag values are considered (Fig. 2).

More extensive exploration of the time series at lead and lag (Table 1) reveals that EOF-1 has maximum correlation of 0.80 with Niño-3.4 index, with EOF-1 lagging by 4 months (versus 0.61 at zero lag), while EOF-2 leads the Niño-3.4 index by 2 months (correlation 0.68, versus 0.64 at zero lag). However, with the Southern Oscillation index (SOI), the maximum correlation

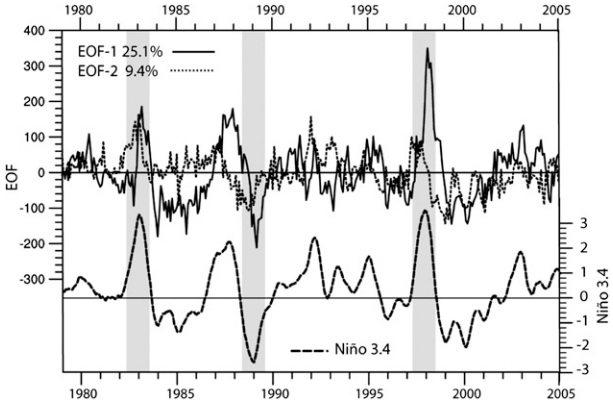

FIG. 1. Time series for EOF-1 (solid), EOF-2 (dotted), left axis; and the Niño-3.4 SST index (dashed), right axis. Vertical light gray bars highlight the biggest ENSO events to show the relative alignments.

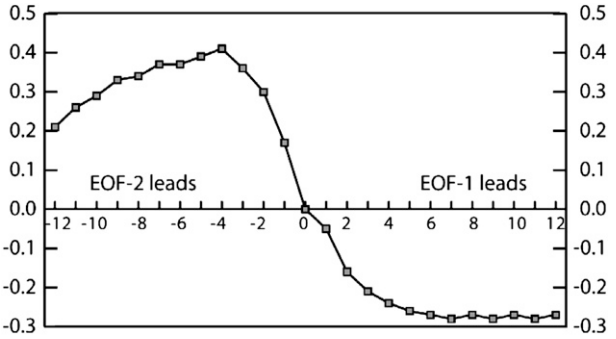

FIG. 2. Cross correlation of EOF-1 with EOF-2 at various leads and lags in months.

with EOF-2 is at zero lag (−0.73). As correlations with TNI are more modest and occur at about 10–12 months leads by TNI, the TNI-related (or El Niño Modoki) patterns do not play a major role here. EOF-1 is also correlated 0.45 with global mean surface temperatures, whereas EOF-2 is negatively correlated −0.28 at zero lag or −0.47 at 5 months lag. Correlations are modest with the North Pacific Index (NPI).

An examination of the EOF variance explained in each month reveals that more than the 8.3% of the variance expected in each of the 12 months occurs in December, January, February, March, April, and May for EOF-1 versus October, November, December, January, February, and March for EOF-2. Hence, while both are active in northern winter, EOF-2 is relatively more active in the northern fall versus EOF-1, which is relatively more active in the northern spring.

From the ENSO event perspective, there is a tendency for a slow buildup of EOF-2 a year or so in advance of a more rapid buildup of EOF-1. EOF-2 rises or falls to peak values in only 4–6 months, but then features a more rapid decline leading EOF-1 by about 4 months, except for the 1997/98 event. The peaks in EOF-1 are close to January or February, while EOF-2 often peaks 6–10 months in advance, as early as in the previous northern spring.

b. EOF results: Vertical structure

The zonal mean temperature structure in the two EOFs (Fig. 3) reveals the deep vertical mode for EOF-1, with strong tropospheric warming corresponding to El Niño conditions and extending from the surface to 100 hPa and with a related reversal in sign in the lower stratosphere centered at 70 hPa. Correlations exceed 0.8 at 500 hPa and are above 0.7 from 700 to 150 hPa and within ±15° latitude of the equator. The actual structure is one similar to the moist adiabatic lapse rate with maximum temperature changes near 200 hPa. EOF-2 correlations exceed 0.2 near 25° to 30° latitude in both hemispheres, with coherent structure from the surface to 150 hPa, and a reversal in sign from 100 to 70 hPa. But the zonal mean values are not strong as there is strong cancellation owing to the wave structure.

The spatial structures are illustrated at only selected levels for 1000, 500, 200, and 100 hPa in Figs. 4 and 5 for all months together and Figs. 6 and 7 for the extended seasons. At 1000 hPa the values over the ocean correspond very closely to those for observed SST anomalies, which is expected as the SSTs fields are specified as lower boundary conditions for the reanalyses.

For EOF-1 (Figs. 4 and 6), as for ERA-40 (Trenberth and Smith 2006), the 1000- and 850-hPa levels feature a boomerang-shaped cooler region from the North Pacific to the western tropical Pacific and to the South Pacific surrounding the warm temperatures from the date line to the Americas in the tropics. Comparable warmth in terms of the correlations occurs in the tropical Indian Ocean and western Atlantic. Teleconnected wave patterns are evident across the South Pacific from New Zealand to South America and from the North Pacific to North America. At 700 and 500 hPa, the temperature anomalies are much more zonal, with maxima throughout

TABLE 1. Maximum correlation between monthly anomaly EOF time series and climate indices for 1979–2004. The lead or lag in months is given in parentheses with a positive value meaning the EOF time series leads. All values are statistically significant.

	Niño-3.4	SOI	TNI	NPI	Global surface temperature	EOF-2
EOF-1	0.80 (−4)	−0.57 (−4)	−0.32 (−12)	−0.20 (−2)	0.45 (0)	0.41 (−4)
EOF-2	0.68 (+2)	−0.73 (0)	−0.34 (−10)	−0.27 (0)	−0.51 (−7)	

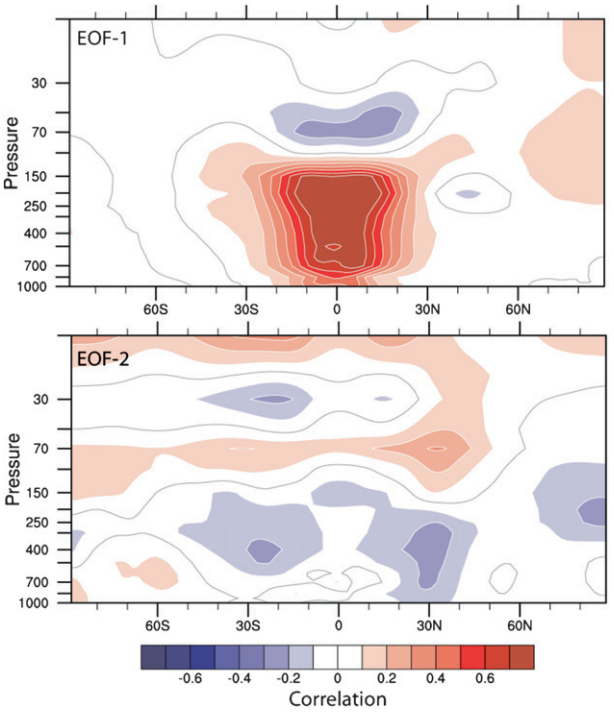

FIG. 3. Cross sections of zonal mean temperature anomaly correlations with EOF-1 and -2 time series. The contour interval is 0.1.

the tropics. The magnitude grows from 300 to 200 hPa, but by 100 hPa the quadrupole signature of Rossby waves straddling the equator emerges, with temperatures below average in the eastern Pacific and above average over the western tropical Pacific. To some extent this is the reverse of the pattern near the surface. The patterns for all months (Fig. 5) are reflected in those for NDJFM (Fig. 6), whereas the wave structures are somewhat weaker for the MJJAS season (Fig. 6).

The spatial structure of EOF-2 (Figs. 5 and 7) also reveals the tropospheric warming in the tropical eastern Pacific but with broader meridional extent, extending from Alaska to Patagonia, and again the NDJFM season is most similar to the pattern over all months. At 1000 hPa and in SSTs (not shown), the boomerang structure or reversed-sign temperature anomaly in the western Pacific is also evident but is much stronger and more extensive than for EOF-1. In this pattern, during El Niño conditions, cool conditions prevail over the tropical Indian Ocean and extend throughout southern Asia and tropical Africa and the Atlantic. Much the same pattern occurs at 850 hPa, but by 500 hPa the pattern is quite different, although striking. The emphasis is on off-equatorial centers that straddle the equator as a quadrupole pattern with opposite-signed centers over the Indian Ocean and southern Asia versus the central

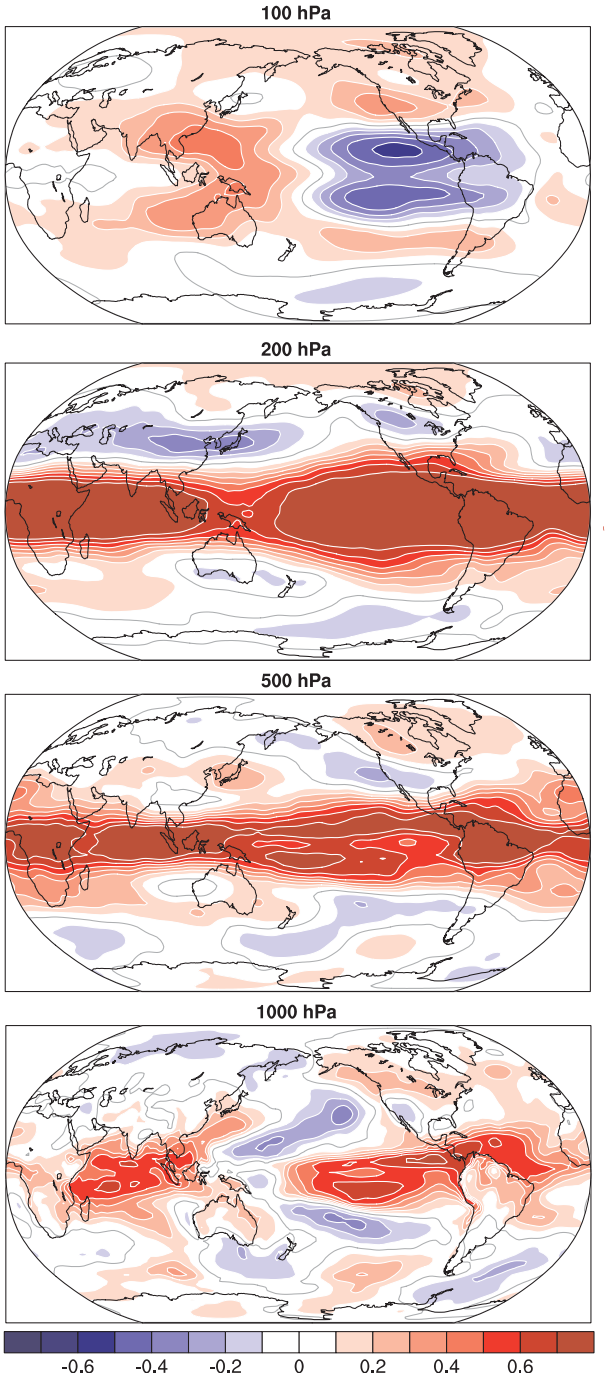

FIG. 4. EOF-1 correlation maps of temperature anomalies at 1000, 500, 200, and 100 hPa.

Pacific. The latter also link to reverse centers at higher latitudes in both hemispheres. At 300 and 200 hPa (Fig. 6), the dominant features are the warm areas over the North and South Pacific of one sign and the reverse sign anomaly centered over Indonesia. The extent and amplitude of the warm area over the eastern Pacific is much

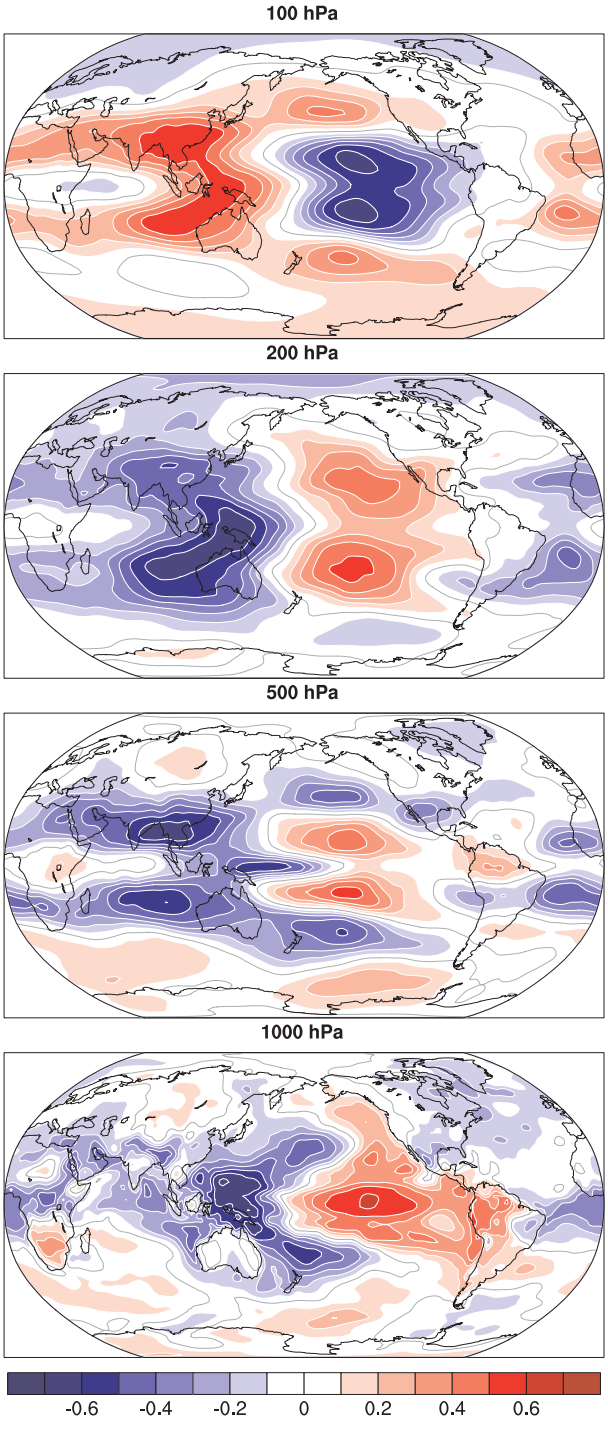

FIG. 5. Same as Fig. 4, but for EOF-2.

less in MJJAS in the mid- and upper troposphere. At 100 hPa, the anomalies are reversed in sign.

c. *Related fields*

To determine the sea level pressure and upper-tropospheric circulation fields associated with these patterns, we have regressed the time series onto the sea level pressure and 300-hPa geopotential height fields, shown for EOF-1 and EOF-2 in Figs. 8 and 9. In these figures, the correlation pattern is shown for all months combined, but the regression to give actual anomaly patterns is given for each of the extended seasons. Both EOF results feature Southern Oscillation (SO)-like sea level pressure patterns but with important differences. For EOF-1 (Fig. 8), the east–west dipole structure is strongest in the equatorial region, as it was for the 1997/98 El Niño. The more classic SO structure with maximum correlations off the equator in the east Pacific and highest in the South Pacific, including the Tahiti area (see Trenberth and Caron 2000), is featured in EOF-2 (Fig. 9). The teleconnection to the North Pacific is clear in both cases but with the EOF-1 pattern featuring an extension toward California, while EOF-2 features a stronger Aleutian low that is somewhat farther west than for EOF-1, and more aligned with the Pacific–North American (PNA) teleconnection pattern.

In the upper troposphere, EOF-1 (Fig. 8) becomes zonal, with high heights in the tropics and strong maxima in the eastern Pacific straddling the equator and teleconnection patterns extending toward higher latitudes in both hemispheres, but fairly weak. The extratropical teleconnections are more statistically significant and much stronger for EOF-2 (Fig. 9), with major changes over the North Pacific and North American region. In the North Pacific at 300 hPa in northern winter, as part of the PNA, the height anomalies for EOF-2 for a one standard deviation anomaly exceed 50 gpm. A very strong wave 1 occurs in the Southern Hemisphere for EOF-2 (anomalies −35 gpm per standard deviation), while EOF-1 projects more onto wave 3.

Regressions of the EOF time series with precipitation have been made for each month, and the zonal mean results (Fig. 10) reveal that the strongest values occur from November through March in the extended northern winter. Chou and Lo (2007) and Giannini et al. (2007) have noted the asymmetric response of precipitation to ENSO and variations with season. In May (EOF-2) or June (EOF-1) through September the precipitation anomalies are weaker and displaced. Figure 10 provides the main justification for grouping the NDJFM and MJJAS months together. For EOF-1, during the El Niño phase (positive values), the zonal mean precipitation anomaly exceeds 0.7 mm day^{-1} in the equatorial region to 10°S during northern winter, while a strong 0.4 mm day^{-1} opposite anomaly occurs near 10°N, signifying a shift in the ITCZ. A weaker negative anomaly in the Southern Hemisphere is related to changes in the South Pacific convergence zone (SPCZ), but it is not simply meridional. In northern summer, there is less evidence of a dipole

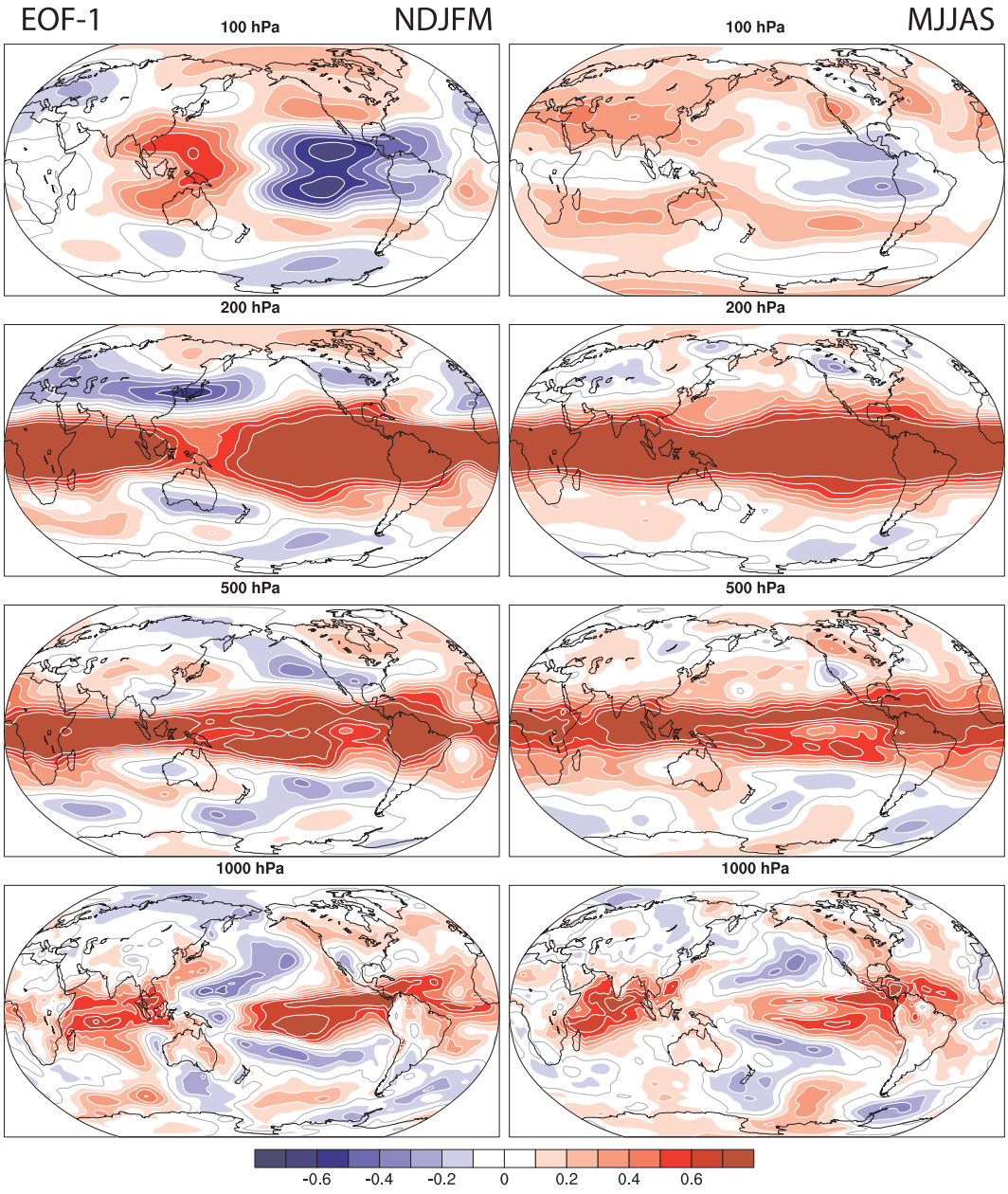

FIG. 6. EOF-1 correlation maps of temperature anomalies at 1000, 500, 200, and 100 hPa for the two extended seasons: (left) NDJFM and (right) MJJAS.

structure and enhanced precipitation occurs near 7°N. Global mean values are positive in all months except January and average 0.013 mm day^{-1}. For EOF-2, once again the dipole structure in northern winter related to the ITCZ shift is evident; it is not as strong and a bit farther south. However, a much stronger decrease in precipitation occurs in the southern tropics throughout the year and is mirrored by a decrease in the northern tropics in boreal summer. The global mean averages -0.014 mm day^{-1} and is negative in all months except January.

The changes in precipitation P are strongly regional in nature (Fig. 11) and remarkably similar between the two EOFs; pattern correlations in NDJFM are 0.86 and in MJJAS 0.29 over the 18 432 global grid points. Significant values are confined to about $\pm 40°$ latitude. The dipole-like structure in the Southern Hemisphere in NDJFM is a signature of the shift in the SPCZ, so there is large cancellation in the zonal mean. The similarities are strong throughout the Pacific and Atlantic. Note also that the magnitudes of the regional changes exceed

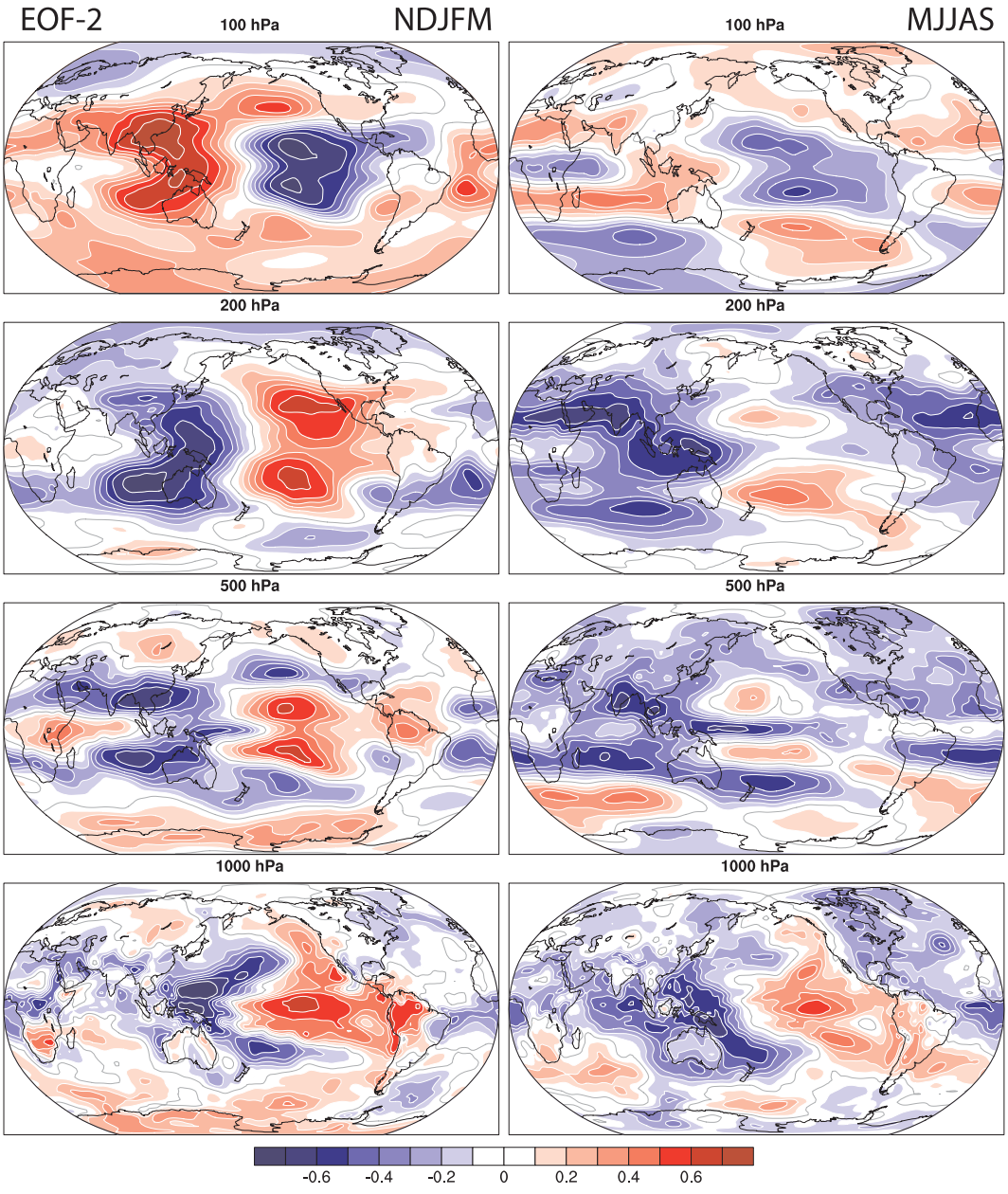

FIG. 7. Same as Fig. 6, but for EOF-2.

2 mm day^{-1} in NDJFM but are about half those values in MJJAS. The main differences (best seen in difference maps, not shown) in NDJFM are over northern Australia and the eastern Indian Ocean where decreases in precipitation are much larger for EOF-2, while there is an increase in precipitation in EOF-1 in the equatorial region from 150°W to Peru. For MJJAS, the largest differences are the much more extensive decreases in precipitation in EOF-2 over Indonesia, the tropical Indian Ocean, and east of China, although with some increases in the southeastern Pacific that extend over Chile.

We have similarly computed the corresponding maps for a number of other quantities, including OLR (Fig. 12), vertical motion (not shown), total vertically integrated diabatic heating Q_1 (Fig. 13), and moistening $Q_2 = E - P$, where E is evaporation. For the JRA reanalyses, Trenberth and Smith (2008) provide a full evaluation and discussion of these terms, which are derived from the energy and moisture budgets, not from the model physics. The $E - P$ is dominated by changes in P, and spatially the OLR and vertical motion changes are similar to those in P as well. For OLR, where the main

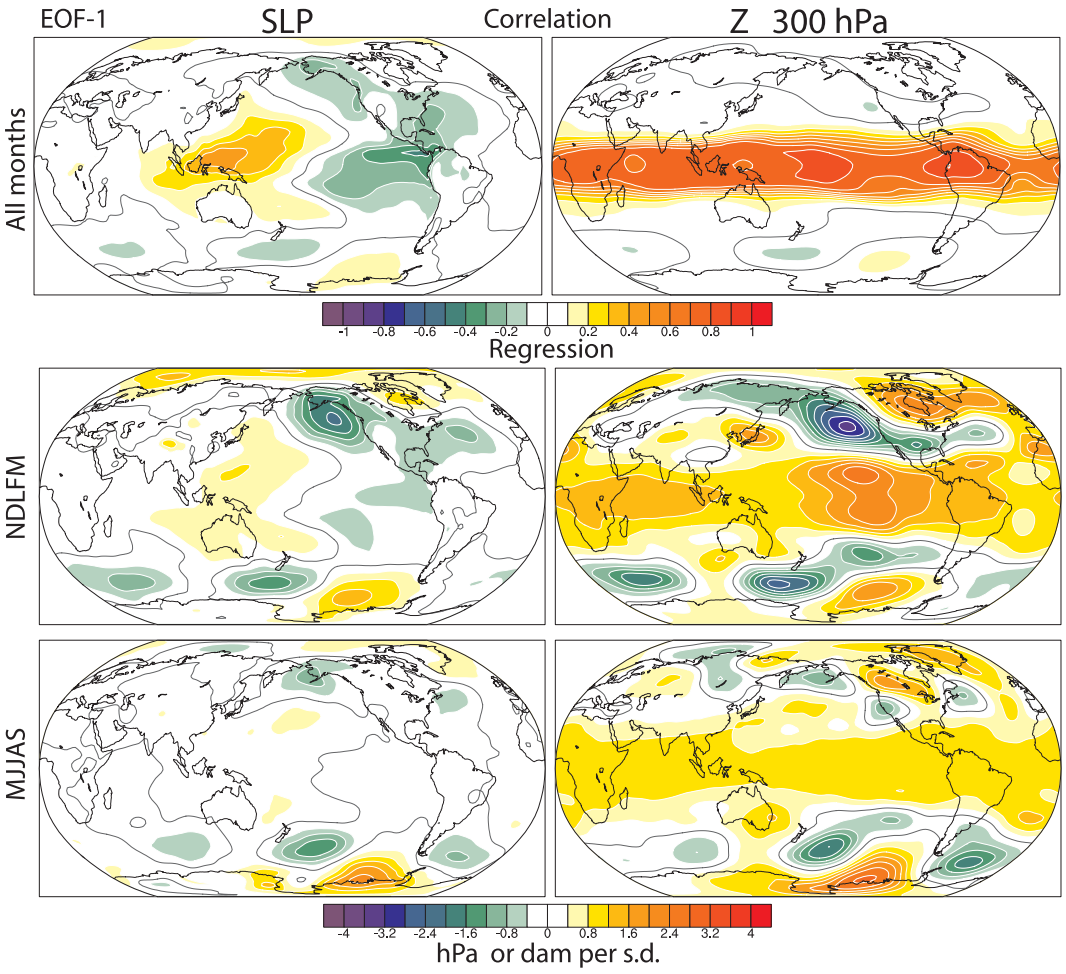

FIG. 8. Patterns for EOF-1 of (top) correlation for all months and (middle),(bottom) regression for NDJFM and MJJAS with (left) sea level pressure and (right) 300-hPa height. The units are hPa (left) or dam (right) per standard deviation of the time series.

signature comes from high cold clouds in association with convection and precipitation, the sign is reversed from the precipitation maps.

The vertically integrated diabatic heating (Fig. 13), which has very similar patterns to those for vertical motion at 500 hPa, signifies the dominance of latent heat from precipitation; values exceed ± 70 W m^{-2} per standard deviation in NDJFM for both EOF-1 and EOF-2. For EOF-1 the maximum is along the equator from 160°E to about 100°W and with maximum cooling in NDJFM near the Philippines for EOF-1 and in the Coral Sea for EOF-2.

4. Discussion and conclusions

The dominance of ENSO in global and tropical variability makes it unsurprising that it dominates the first temperature EOF, but the analysis highlights the fact that there are different flavors of El Niño when the full three-dimensional structure of the atmospheric circulation and temperature field is considered, and more than one EOF is essential to capture the full character of ENSO. EOF-1 captures the core of the 1997/98 El Niño event and projects onto most other events as well, with the exception of the ENSO events in the early 1990s. But EOF-2 is also important for most El Niño events. It was significant in 1997, 10 months before the peak of the event in early 1998. EOF-2 generally builds up in the early stages of ENSO events in the northern summer and fall, while it is mainly in the northern winter when EOF-1 fully blossoms. Thus while the sea level pressure and rainfall patterns have similarities, the vertical structures differ considerably, and the extratropical teleconnections differ.

The dominant pattern (EOF-1), in its positive sign, features highly coherent zonal mean warming throughout

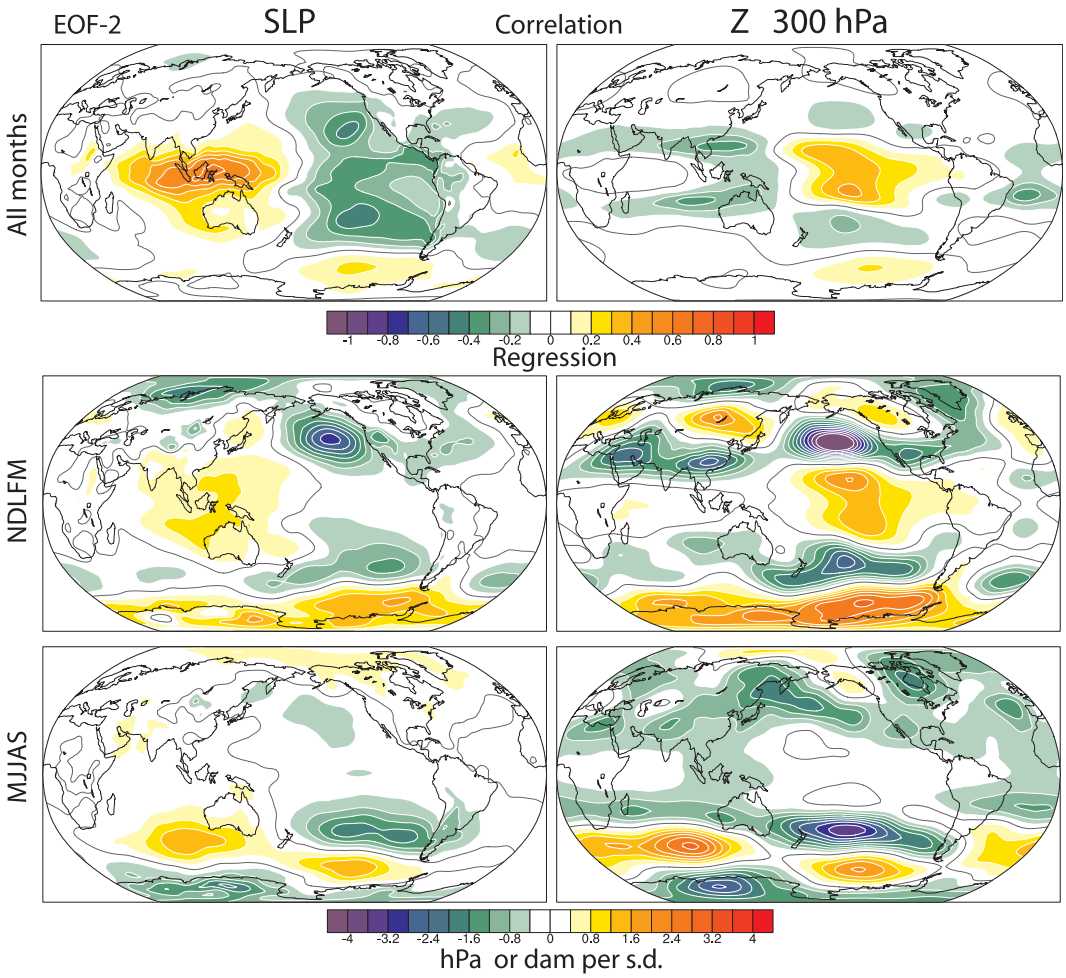

FIG. 9. Same as Fig. 8, but for EOF-2.

the tropical troposphere from 30°N to 30°S that increases in magnitude with height to 300 hPa, drops to zero about 100 hPa at the tropopause, and has reverse sign to 30 hPa with peak negative values at 70 hPa. Warmth dominates throughout most of the tropics although with opposite anomalies in the western tropical Pacific (weak) and Pacific subtropics (strong). Coherent wave structures at higher latitudes cancel out in the zonal mean. The structure is more zonal above about 700 hPa and features off-equatorial maxima straddling the equator in the eastern Pacific in the upper troposphere with opposite sign at 100 hPa. Such a signature is likely one of a thermally forced standing Rossby wave, first noted by Yulaeva and Wallace (1994), although with other mechanisms extending the pattern to midlatitudes, as discussed by Seager et al. (2003).

EOF-2 corresponds more closely with the traditional SO, with more off-equatorial action. In the zonal mean it features weak warming below 700 hPa, cooling from 700 to 300 hPa, and warming above there that peaks at 100 hPa, and extends from 40°N to 50°S. However, the zonal mean is a residual of a much stronger wave pattern that changes sign across about the date line and is fairly coherent throughout the troposphere from the surface through 200 hPa, reversing in sign at 100 hPa. Strong Rossby wave signatures are featured in the troposphere with a distinctive quadrupole pattern that reverses at 100 hPa.

A review of the theory and observations of teleconnections with ENSO (Trenberth et al. 1998) highlights the important role of Rossby waves that emanate from the tropical diabatic forcing in association with SST variations. The main source of diabatic forcing is from latent heat release in precipitation and moist convection (e.g., Chiang and Sobel 2002), and often there are dipole anomaly structures as the convergence zone is moved. Branstator (1985) introduced the idea of a Green's function related to such forcing and found that the response can be very sensitive to tropical forcing position. Certainly our results are surprising as

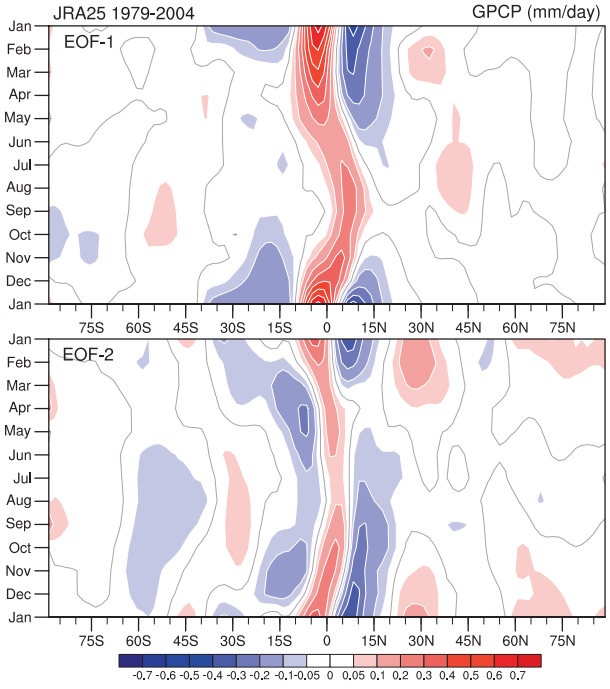

FIG. 10. Regression of the time series with zonal mean precipitation for each month of the year as latitude–time sections for (top) EOF-1 and (bottom) EOF-2. Units are mm day^{-1} per standard deviation of the time series.

to how small the variations in precipitation and diabatic heating are in the two ENSO modes identified here, if they are indeed causal. One reason for the differences is the tendency for EOF-2 to peak in the northern summer or fall, while EOF-1 peaks in northern winter. Giannini et al. (2007) examined the different atmospheric responses to the evolving states of ENSO and noted the differences between northern summer and winter (especially associated with the differences in precipitation in Indonesia), and they suggest that the response is not as coherent in the decay phase of El Niño. Anomalies in precipitation depend mostly on the mean fields and shifts in convergence zones associated with changes in SSTs, and mean fields differ among seasons, with the strongest convergence zones in the summer hemisphere. As well as modest changes in the precipitation and diabatic heating, there are bigger changes in the background wind fields through which the forced Rossby waves propagate, and presumably this factor is important for explaining differences in teleconnections.

Kumar and Hoerling (1997) and Peng and Kumar (2005) noted the sensitivity of the extratropical response to particular El Niño events and associate it with internal atmospheric variability as well as the differences in SSTs, but these other differences likely matter as well. Kumar et al. (2005) analyzed 80 ensemble atmospheric model simulations in response to observed

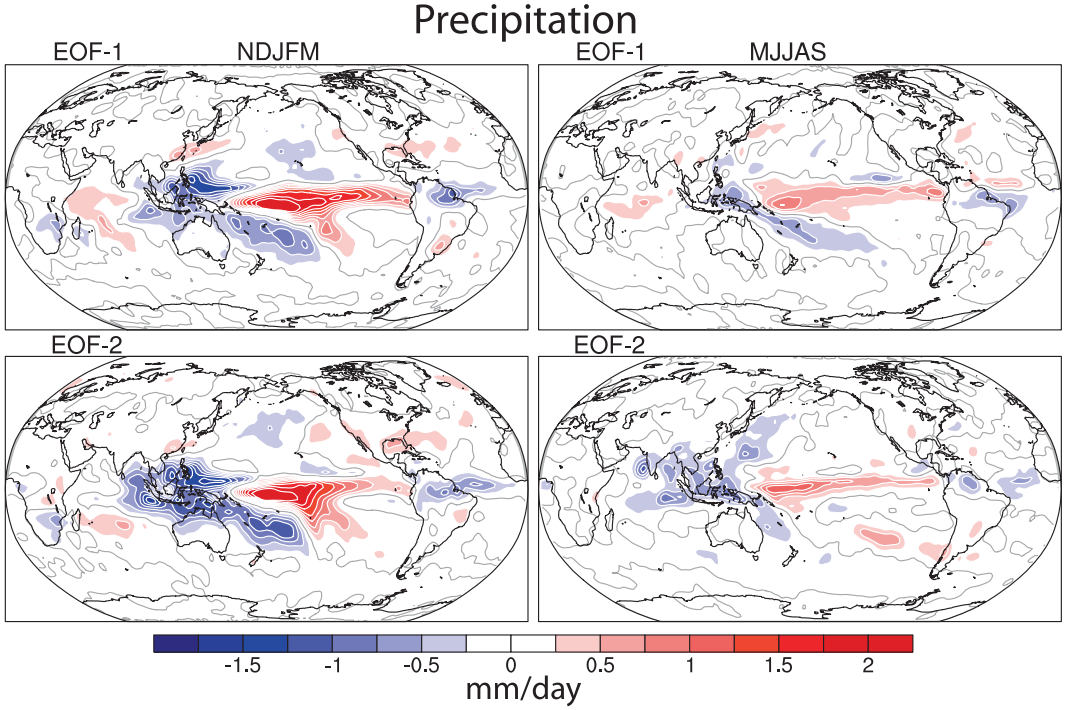

FIG. 11. Precipitation regression of the (left) northern winter months NDJFM and (right) northern summer months MJJAS for (top) EOF-1 and (bottom) EOF-2 in mm day^{-1} per standard deviation of the time series.

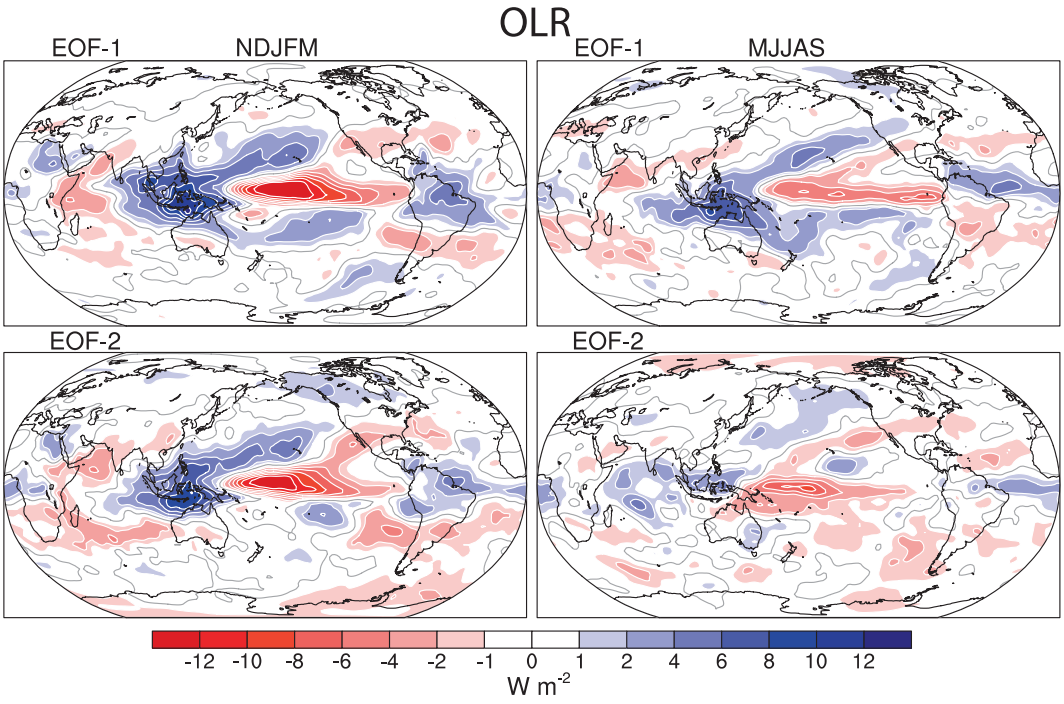

FIG. 12. OLR regression of the (left) northern winter months NDJFM and (right) northern summer months MJJAS for (top) EOF-1 and (bottom) EOF-2 in W m^{-2} per standard deviation of the time series.

SSTs for 1980–2000 but focused on only one season: December–February, and they performed an EOF analysis of 200-hPa geopotential heights. Although their dominant pattern is likely related to our EOF-1, it is not an exact match, and neither the time series nor the spatial structures of their higher modes seem to relate to our EOF-2. Nevertheless, their results suggest that ENSO involves more than one ''mode,'' although whether their model is capable of simulating the different vertical structures in moist convection would need to be ascertained.

EOF-1 depicts ENSO especially as seen in the peak of the 1997/98 El Niño event. It is strongly correlated with the ENSO indexes and lags them by about 4 months. EOF-2 plays a role in most events and tends to occur several months earlier in the events, while EOF-1 follows some 6 months later in the mature phase of deep convection. As El Niño develops, the buildup of heat in the ocean spreads eastward across the Pacific and then poleward along the Americas within the ocean (Trenberth et al. 2002b). At the same time, strong accompanying convection pumps heat into the atmosphere and drives teleconnections throughout the tropics that extend to higher latitudes (Trenberth et al. 2002a,b; Chiang and Lintner 2005). In the tropics, the overturning atmospheric circulation creates subsidence and clear skies over the tropical Indian and Atlantic Oceans, which subsequently warm, and peak several months after Niño-3.4 SSTs (evident in EOF-1), as described by Klein et al. (1999). The general heating of the atmosphere also leads to a miniglobal warming which peaks, on average, three months after the peak in Niño-3.4 SSTs at the surface, as also is discussed by Kumar and Hoerling (2003) and Chiang and Lintner (2005). EOF-1 captures much of this behavior. In the deep tropics, it features an increase in amplitude of temperature perturbation with height, consistent with the dominant process of moist convection and the moist adiabatic lapse rate, and as seen in models (Santer et al. 2005). The peak temperature magnitude is at 300 hPa and drops to zero at the tropopause. The temperature anomalies reverse sign in the lower stratosphere, also consistent with being driven from below and the signal is confined to below about 30 hPa. Regionally, the Rossby wave dipole response in the Pacific, with reversed sign at 100 and 50 hPa, is also consistent with previous understanding and model results.

EOF-2, however, depicts an alternative temperature structure to that in EOF-1 for ENSO and highlights the sequence of 3 successive El Niño events in the early 1990s. Its presence belies the findings from earlier climate models that seem to prefer a single deterministic structure in response to El Niño (Kumar and Hoerling 1997). EOF-2 features more decadal variability and somewhat longer

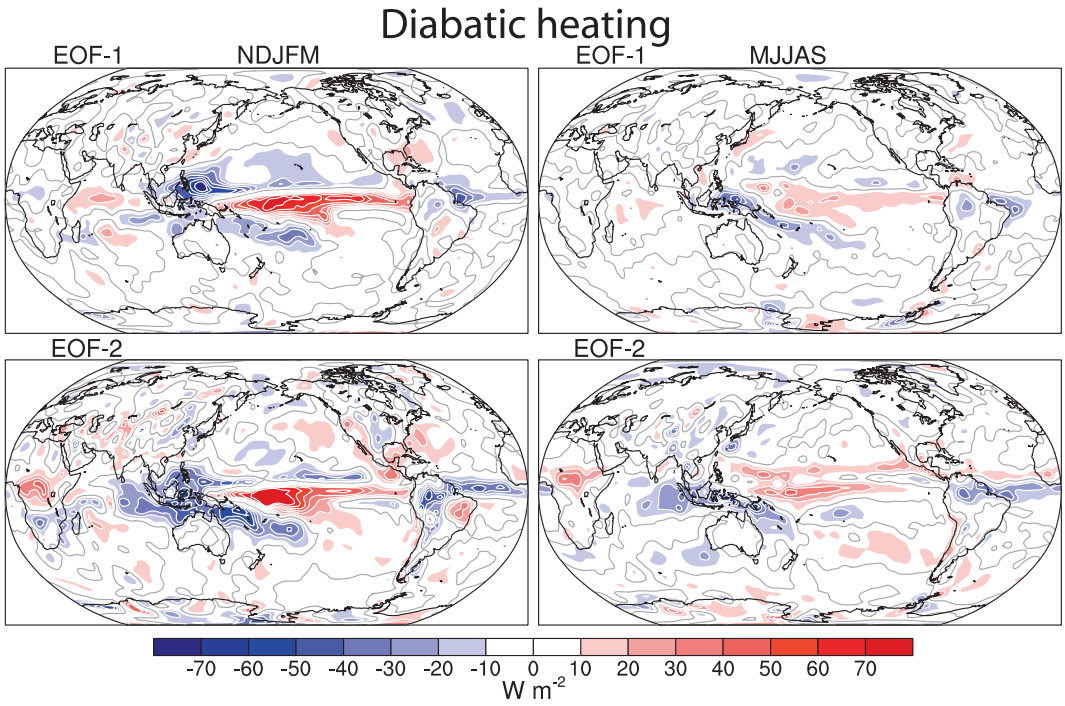

FIG. 13. Vertically integrated diabatic heating Q_1 regression of the (left) northern winter months NDJFM and (right) northern summer months MJJAS for (top) EOF-1 and (bottom) EOF-2 in W m^{-2} per standard deviation of the time series.

time scales, and much broader structures meridionally in the Pacific, as previously identified with Pacific decadal variability (Zhang et al. 1997; Garreaud and Battisti 1999). This pan-Pacific pattern is dominated by Southern Oscillation wave 1 structures throughout the tropics and subtropics, and the strongest values in the Pacific extend well into the extratropics. The distinctive quadrupole pattern that reverses at 100 hPa likely indicates Rossby wave effects. There is little contribution to global mean surface temperature values.

A key difference, then, between EOF-1 and EOF-2 is the extent of the warming throughout the troposphere and globally in EOF-1. EOF-1 is predominant in the late stages of an El Niño event when excess heat is being lost by the ocean in the form of evaporative cooling to the atmosphere (Trenberth et al. 2002b) and realized in the atmosphere as latent heating in deep convection. EOF-2 instead features net atmospheric warming and diabatic heating in its negative phase, that of La Niña, when precipitation is heaviest over Indonesia and northern Australia (Fig. 11). The strong tendency for EOF-2 to lead EOF-1 also suggests a precursor before the deep convection of EOF-1, with key indicators related to the amount of heat being lost by the ocean and the extent to which moisture increases in the atmosphere (Trenberth et al. 2005) and precipitation increases in the tropics (Gu et al. 2007), both signatures of the major El Niño events.

The changes in the extratropics and thus in the storm tracks between EOF-1 and EOF-2 are substantial. While there is some shift eastward in the diabatic heating in El Niño in the central Pacific with EOF-1, the biggest differences actually lie over the eastern Indian Ocean and far west tropical Pacific, where much greater cooling coincides with an anomalous decrease in precipitation in EOF-2. It seems likely that such negative heating anomalies may play a more important role in El Niño teleconnections than has generally been appreciated.

The quite different three-dimensional structure of these different ENSO patterns highlights the need to consider the seasonal variations and the full structure outside of the Pacific at all levels, as well as the relationship to the global mean. It also suggests the important role of the annual cycle and the seasonal variations on which these variations are imposed and nonlinearities may be involved (Hoerling et al. 1997). These factors should be considerations in predictions, whether using analogs and statistical methods, or models. Are models capable of reproducing the variety of vertical structures observed? A key diagnostic of the transition from EOF-2 to EOF-1 may be the net evaporation (and ocean heat lost) in the tropical Pacific along with the total precipitation and atmospheric latent heating in deep moist convection that result in different teleconnections into the extratropics.

Acknowledgments. This research is partially sponsored by the NOAA CLIVAR and CCDD programs under Grants NA07OAR4310051 and NA06OAR4310145.

REFERENCES

Ashok, K., S. K. Behera, S. A. Rao, H. Weng, and T. Yamagata, 2007: El Niño Modoki and its possible teleconnection. *J. Geophys. Res.,* **112,** C11007, doi:10.1029/2006JC003798.

Branstator, G., 1985: Analysis of general circulation model sea-surface temperature anomaly simulations using a linear model. Part I: Forced solutions. *J. Atmos. Sci.,* **42,** 2225–2241.

Chiang, J. C. H., and A. H. Sobel, 2002: Tropical tropospheric temperature variations caused by ENSO and their influence on the remote tropical climate. *J. Climate,* **15,** 2616–2631.

——, and B. R. Lintner, 2005: Mechanisms of remote tropical surface warming during El Niño. *J. Climate,* **18,** 4130–4149.

Chou, C., and M. H. Lo, 2007: Asymmetric responses of tropical precipitation during ENSO. *J. Climate,* **20,** 3411–3433.

Garreaud, R. D., and D. S. Battisti, 1999: Interannual (ENSO) and interdecadal (ENSO-like) variability in the Southern Hemisphere tropospheric circulation. *J. Climate,* **12,** 2113–2123.

Giannini, A., A. W. Robertson, and J.-H. Qian, 2007: A role for tropical tropospheric temperature adjustment to El Niño–Southern Oscillation in the seasonality of monsoonal Indonesia precipitation predictability. *J. Geophys. Res.,* **112,** D16110, doi:10.1029/2007JD008519.

Gu, G., R. F. Adler, G. J. Huffman, and S. Curtis, 2007: Tropical rainfall variability on interannual-to-interdecadal and longer time scales derived from the GPCP monthly product. *J. Climate,* **20,** 4033–4046.

Hoerling, M. P., A. Kumar, and M. Zhong, 1997: El Niño, La Niña, and the nonlinearity of their teleconnections. *J. Climate,* **10,** 1769–1786.

Kao, H.-Y., and J.-Y. Yu, 2009: Contrasting eastern-Pacific and central-Pacific types of ENSO. *J. Climate,* **22,** 615–632.

Klein, S. A., B. J. Soden, and N. C. Lau, 1999: Remote sea surface temperature variations during ENSO: Evidence for a tropical atmospheric bridge. *J. Climate,* **12,** 917–932.

Kumar, A., and M. P. Hoerling, 1997: Interpretation and implications of the observed inter–El Niño variability. *J. Climate,* **10,** 83–91.

——, and ——, 2003: The nature and causes for the delayed atmospheric response to El Niño. *J. Climate,* **16,** 1391–1403.

——, Q. Zhang, P. Peng, and B. Jha, 2005: SST-forced atmospheric variability in an atmospheric general circulation model. *J. Climate,* **18,** 3953–3967.

Kumar, K. K., B. Rajagopalan, M. Hoerling, G. Bates, and M. Cane, 2006: Unraveling the mystery of Indian monsoon failure during El Niño. *Science,* **314,** 115–119.

Onogi, K., and Coauthors, 2007: The JRA-25 Reanalysis. *J. Meteor. Soc. Japan,* **85,** 369–432.

Peng, P., and A. Kumar, 2005: A large ensemble analysis of the influence of tropical SSTs on seasonal atmospheric variability. *J. Climate,* **18,** 1068–1085.

Santer, B. D., and Coauthors, 2005: Amplification of surface temperature trends and variability in the tropical atmosphere. *Science,* **309,** 1551–1556.

Seager, R., N. Harnik, Y. Kushnir, W. Robinson, and J. Miller, 2003: Mechanisms of hemispherically symmetric climate variability. *J. Climate,* **16,** 2960–2978.

Trenberth, K. E., and T. J. Hoar, 1996: The 1990–1995 El Niño–Southern Oscillation event: Longest on record. *Geophys. Res. Lett.,* **23,** 57–60.

——, and ——, 1997: El Niño and climate change. *Geophys. Res. Lett.,* **24,** 3057–3060.

——, and J. M. Caron, 2000: The Southern Oscillation revisited: Sea level pressures, surface temperatures, and precipitation. *J. Climate,* **13,** 4358–4365.

——, and D. P. Stepaniak, 2001: Indices of El Niño evolution. *J. Climate,* **14,** 1697–1701.

——, and L. Smith, 2006: The vertical structure of temperature in the tropics: Different flavors of El Niño. *J. Climate,* **19,** 4956–4970.

——, and ——, 2008: Atmospheric energy budgets in the Japanese Reanalysis: Evaluation and variability. *J. Meteor. Soc. Japan,* **86,** 579–592.

——, G. W. Branstator, D. Karoly, A. Kumar, N.-C. Lau, and C. Ropelewski, 1998: Progress during TOGA in understanding and modeling global teleconnections associated with tropical sea surface temperatures. *J. Geophys. Res.,* **103,** 14 291–14 324.

——, D. P. Stepaniak, and J. M. Caron, 2002a: Interannual variations in the atmospheric heat budget. *J. Geophys. Res.,* **107,** 4066, doi:10.1029/2000JD000297.

——, J. M. Caron, D. P. Stepaniak, and S. Worley, 2002b: Evolution of El Niño–Southern Oscillation and global atmospheric surface temperatures. *J. Geophys. Res.,* **107,** 4065, doi:10.1029/2000JD000298.

——, J. Fasullo, and L. Smith, 2005: Trends and variability in column-integrated water vapor. *Climate Dyn.,* **24,** 741–758.

Uppala, S. M., and Coauthors, 2005: The ERA-40 Re-Analysis. *Quart. J. Roy. Meteor. Soc.,* **131,** 2961–3012.

Yulaeva, E., and J. M. Wallace, 1994: The signature of ENSO in global temperature and precipitation fields derived from the Microwave Sounding Unit. *J. Climate,* **7,** 1719–1736.

Zhang, Y., J. M. Wallace, and D. S. Battisti, 1997: ENSO-like interdecadal variability: 1900–93. *J. Climate,* **10,** 1004–1020.